ROYAL SOCIETY OF CHEMISTRY

PAPER

Check for updates

Light-driven efficient dry reforming of methane over Pt/La$_2$O$_3$ with long-term durability†

Yanxia Gao,[abce] Qiang Li,[abce] Chunqi Wang,[abce] Dongxu Yan,[abce] Jing Chen [ID][de] and Hongpeng Jia [ID] *[abce]

The instability caused by coking and catalyst sintering during the dry reforming of methane (DRM) is a major obstacle to their commercialization. Herein, Pt/La$_2$O$_3$ exhibits high yield of syngas and satisfactory durability of at least 200 h during the DRM reaction under focused light illumination without external heating, and no obvious aggregation occurs to Pt nanoparticles on Pt/La$_2$O$_3$. The H$_2$ production rate of 1284.5 mmol g$_{cat}^{-1}$ h^{-1} and the selectivity of ~0.89 in photothermocatalysis are 3.0 and 2.1 folds of those in the thermocatalysis at the same temperature (700 °C), respectively. Light-excited hot electrons and more oxygen vacancies accelerate the spontaneous desorption of H$_2$ and the activation and dissociation of CH$_4$ and CO$_2$ to improve the catalytic performance, which together with the strong Pt-support interaction contributes to the reaction stability. The stable catalyst design can be extended to other harsh reactions, offering great potential for industrial applications.

1. Introduction

The dry reforming of methane (DRM), an environmental and economic strategy to convert greenhouse gases CO$_2$ and CH$_4$ into syngas (H$_2$ and CO), is applied in the synthesis of valuable chemicals and value-added liquid fuels, and provides promising tactics for solving energy shortages.[1,2] Among various technologies, photothermocatalytic DRM, driven by solar irradiation without external heating and stored solar energy into chemicals, is an effective and attractive technique with low or zero energy consumption of photocatalysis and high catalytic efficiency of thermocatalysis.[3–5] Although numerous catalysts have been exploited for DRM, it still remains a major challenge for catalyst deactivation caused by sintering and coking during the DRM reaction, particularly for group VIII metal-based catalysts.[6,7]

Photothermocatalysts possess strong light absorption capacity and high thermocatalytic activity, which promotes photothermocatalytic DRM.[8] Pt nanoparticles (NPs) exhibit

[a]Xiamen Key Laboratory of Materials for Gaseous Pollutant Control, Institute of Urban Environment, Chinese Academy of Sciences, Xiamen 361021, China

[b]Key Laboratory of Urban Pollutant Conversion, Institute of Urban Environment, Chinese Academy of Sciences, Xiamen 361021, China

[c]CAS Center for Excellence in Regional Atmospheric Environment, Institute of Urban Environment, Chinese Academy of Sciences, Xiamen 361021, China

[d]Fujian Institute of Research on The Structure of Matter, Chinese Academy of Sciences, Fuzhou 350002, China

[e]University of Chinese Academy of Sciences, Beijing 100049, China. E-mail: hpjia@iue.ac.cn; Fax: +86-592-6190767; Tel: +86-592-6190767

† Electronic supplementary information (ESI) available. See https://doi.org/10.1039/d2ta04246k

strong light absorption according to localized surface plasmon resonance (LSPR) and high catalytic activity, which is expected to be developed as an efficient photothermocatalyst for DRM.[9–12] At 550 °C, the catalytic activity of Pt/TaN for DRM under visible light illumination was enhanced 2.7 folds compared to only thermal catalysis.[10] Pt NPs on mesoporous CeO$_2$ have appreciable production rates of syngas under focused light irradiation with generation rates of 342.0 and 360.0 mmol g$_{cat}^{-1}$ h^{-1} for H$_2$ and CO, respectively.[13] These studies have made progress in the yield of syngas, while further improvement is still needed to effectively achieve reaction stability. CH$_4$ cracking is the main inevitable source of coke deposition that leads to catalyst degradation in photothermocatalytic DRM due to which CO disproportionation is inhibited by photoactivation.[8] Simultaneously, catalyst deactivation is also compromised by the sintering of a metal or support in a hostile environment with reducing atmosphere and high temperature.[14,15] Efficient and stable catalysts have to be fabricated to support the practical application. Some important studies have demonstrated that strong metal-support interaction (SMSI) contributes to improved catalyst stability, catalytic activity, and control reaction selectivity.[16–18] Based on highly crystalline and nanoporous hexagonal boron nitride 2D materials, the construction of non-oxide-derived SMSI nanocatalyst exhibits high catalytic efficiency and durability in CO oxidation under simulated to realistic exhaust systems.[19] The Ru–MoO$_3$ catalyst with SMSI can achieve the selective CO$_2$ hydrogenation to CO with excellent activity and catalytic stability.[20] Therefore, it is expected to fulfill highly-efficient photothermocatalytic DRM on robust catalysts based on strong Pt-support interaction.

Herein, we report Pt NPs supported on La_2O_3 (Pt/La_2O_3) by constructing strong Pt-support interaction as an highly efficient photothermocatalyst for the DRM reaction. Under focused full spectrum light irradiation without additional heating, Pt/La_2O_3 exhibits high generation rate of H_2 (r_{H_2} = 1284.5 mmol g_{cat}^{-1} h^{-1}) and selectivity ($\sim$0.89), which shows nearly 3.0 or 2.1-fold enhancement of those (r_{H_2} = 429.6 mmol g_{cat}^{-1} h^{-1}; selectivity = $\sim$0.43) for thermocatalysis at the same temperature (700 °C), respectively. Also, the production rate of syngas on Pt/La_2O_3 is stable for at least 200 h during the photothermocatalytic reaction. Pt/La_2O_3 exhibits high durability owing to the synergistic effect of strong Pt-support interaction and the oxygen vacancies contribute to the suppression of Pt NPs aggregation and carbon deposition. The physiochemical characterizations and *in situ* diffuse reflectance infrared Fourier transform spectra (DRIFTS) reveal that light irradiation excites more hot electrons and oxygen vacancies, which accelerates the conversion of CH_4 and CO_2 and the desorption of formed H_2, and further promotes the catalytic performance. This work provides a method for achieving highly-efficient photothermocatalytic DRM on stable catalysts by exploiting the synergistic effect of SMSI and oxygen vacancies.

2. Experimental section

2.1 Materials

All following chemical reagents were used directly without further purification: lanthanum nitrate ($La(NO_3)_3 \cdot 6H_2O$) (A. R.), citric acid monohydrate ($C_6H_8O_7 \cdot H_2O$) (A. R.), sodium borohydride ($NaBH_4$) (A. R.), polyvinylpyrrolidone K30 (PVP) (GR), acetone (A. R.), methanol (A. R.), hexane (A. R.), and chloroplatinic acid ($H_2PtCl_6 \cdot 6H_2O$, 38 wt% content of Pt).

2.2 Catalyst preparation

Polyvinylpyrrolidone K30 (PVP)-stabilized Pt NPs were synthesized through the reported method and the detailed procedure is displayed in the ESI.†[21] The solution of $La(NO_3)_3 \cdot 6H_2O$ (8.66 g) and $C_6H_8O_7 \cdot H_2O$ (8.40 g) was treated in a stainless-steel autoclave at 180 °C for 12 h and the obtained La_2O_3 precursor was dried at 80 °C. La_2O_3 was obtained by calcining the La_2O_3 precursor in air at 750 °C for 4 h.

Pt NPs (theoretical loading of 5 wt%) supported on La_2O_3 were synthesized through the following steps: a certain amount of PVP-stabilized Pt NPs solution was dissolved into 100 mL water solution containing La_2O_3 precursor and stirred at 80 °C until the water was completely evaporated. The obtained sample was first heated in nitrogen (N_2) atmosphere and then treated in air atmosphere at 750 °C for 4 h. Finally, the powder was reduced by 10% H_2/Ar (30 mL min^{-1}) at 500 °C for 1 h to obtain Pt/La_2O_3.

Pt/La_2O_3–S was prepared by impregnation. In detail, 500 mg La_2O_3 was dispersed into 100 mL deionized water, and then 6.93 mL H_2PtCl_6 aqueous solution (3.8 mg mL^{-1}) was added. Subsequently, 10 mL $NaBH_4$ aqueous solution (3.5 mg mL^{-1}) was dropped into the above mixture with stirring, and then the obtained suspension was continuously stirred for 3 h. After filtering and drying, the precipitate was calcinated at 750 °C for 4 h in air. Finally, the obtained powder was reduced by 10% H_2/Ar (30 mL min^{-1}) at 500 °C for 1 h to obtain Pt/La_2O_3–S. Based on inductively coupled plasma-optical emission spectroscopy (ICP-OES) measurements (Table S1†), the actual Pt content on Pt/La_2O_3 and Pt/La_2O_3–S is 4.84 and 4.24 wt%, respectively.

2.3 Characterization

The catalysts were characterized by the following techniques: inductively coupled plasma-optical emission spectroscopy (ICP-OES), X-ray diffraction (XRD), high resolution transmission electronic microscopy (HRTEM), energy dispersive X-ray spectroscopy (EDS), thermogravimetric analyzer (TG) analysis, X-ray photoelectron spectroscopy (XPS), electron paramagnetic resonance (EPR), diffuse reflection absorption spectroscopy (DRS), *in situ* diffuse reflectance infrared Fourier transform spectroscopy (DRIFTS), and chemisorption characterization including CO_2 temperature-programmed desorption (CO_2-TPD), CH_4 temperature-programmed desorption (CH_4-TPD), CO temperature-programmed desorption (CO-TPD), H_2 temperature-programmed desorption (H_2-TPD), CO_2 temperature-programmed surface reaction (CO_2-TPSR), CH_4 temperature-programmed surface reaction (CH_4-TPSR), and CH_4/CO_2 temperature-programmed surface reaction (CH_4/CO_2-TPSR).

In H_2-TPD, 50 mg samples were firstly pretreated at 400 °C for 1 h in the flow of 30 mL min^{-1} Ar, then cooled to 40 °C in Ar atmosphere, followed by 5% H_2/Ar flow (adsorption gas, 30 mL min^{-1}) for 1 h under dark or light. After adsorption, Ar gas (30 mL min^{-1}) was switched to purge the weakly adsorbed H_2 for 1 h. Finally, the TPD signal was monitored by the TCD detector and mass spectroscopy through the temperature elevated to 850 °C at 10 °C min^{-1} in an Ar flow of 30 mL min^{-1}.

CO-TPD was performed in the follow procedures. First, 50 mg of the sample was treated with 30 mL min^{-1} helium (He) at 400 °C for 1 h and then cooled to 40 °C. Subsequently, 5% CO/He was introduced for 1 h under dark or light irradiation conditions, followed by purging with He at the same temperature for 1 h. Finally, the temperature eventually rose to 850 °C at 10 °C min^{-1} in He flow of 30 mL min^{-1}, and the desorbed gas signal was detected by the TCD detector and mass spectroscopy.

CO_2-TPD and CH_4-TPD were operated through similar steps as that of CO-TPD, in which the adsorbed gas of 5% CO_2/He and 5% CH_4/He was introduced, respectively.

CO_2-TPSR and CH_4-TPSR were carried out through a similar procedure as follows: 50 mg catalysts were firstly pretreated in flowing He (30 mL min^{-1}) at 400 °C for 1 h, and subsequently cooled down to 40 °C under He gas flow (30 mL min^{-1}). Then, the pre-treated sample with or without pre-illumination under light was heated to 850 °C at 10 °C min^{-1} at a flow of 5% CO_2/He and 10% CH_4/He, respectively. The signal was recorded by mass spectroscopy.

The CH_4/CO_2-TPSR data were obtained through the similar CO_2-TPSR and CH_4-TPSR procedures. The signal was recorded by mass spectroscopy when the pre-treated sample was heated to 850 °C in 10 °C min^{-1} with a $CH_4/CO_2/Ar$ (8/8/84 vol%) flow of 30 mL min^{-1}.

This journal is © The Royal Society of Chemistry 2022

J. Mater. Chem. A, 2022, **10**, 16016–16028 | **16017**

In situ diffuse reflectance infrared Fourier transform spectra (DRIFTS) at room temperature or 400 °C under dark or in irradiation of full-spectrum light were collected on a Bruker Vertex 70 spectrometer equipped with a mercury cadmium telluride (MCT) detector at a resolution of 4 cm^{-1} over 32 scans. The samples were first heated *in situ* at 400 °C under flowing He for 1 h, then cooled to room temperature prior to the recording of background spectra. Subsequently, 8/8/84 vol% CH$_4$/CO$_2$/Ar was introduced into the sample for 10 min. The spectra of CH$_4$ and CO$_2$ absorbed on the sample were recorded at ambient temperature. Then, the temperature was elevated to 400 °C at 10 °C min^{-1} in dark or under light irradiation, and maintained at 400 °C for 1 h while recording the DRIFTS spectra.

The other detailed procedures of characterization are described in the ESI.†

2.4 Activity evaluation

The photothermocatalytic DRM on the samples under the focused light irradiation from a 300 W Xe lamp (PLS-SXE3000UV, Beijing PerfectLight Technology Co. Ltd.) without external heating was conducted on a stainless-steel reactor with a quartz window. The light spot was focused about 5 mm to the sample through a Fresnel lens ($\varphi = 9$ cm). The infrared and UV-vis light were obtained using a cutoff filter. The photothermocatalytic activity of all the samples was carried studied under the same conditions with the power of the focused full-spectrum irradiation of 3.81 W, which was detected by an optical power meter. Also, the intensity of the focused illumination was about 19.42 W cm^{-2}. For all the experiments, a stream of 8/8/84 vol% CH$_4$/CO$_2$/Ar constantly flowed at a flow

Thermal catalytic activities were determined in a tube-type resistance furnace. Typically, 5 mg of the catalysts and 1 g silica sand were loaded in a quartz tube, and 8/8/84 vol% CH$_4$/CO$_2$/Ar at a flow rate of 90 mL min^{-1} was introduced.

Eqn (1) and (2) were applied to calculate the production rate of H$_2$ (r_{H_2}) or CO (r_{CO}) and the conversion rate of CH$_4$ (r_{CH_4}) or CO$_2$ (r_{CO_2}).

$$r_{H_2}(\text{or } r_{CO}) = \frac{n_{H_2}(\text{or } n_{CO})}{\text{Weight of catayst}} \times 60 \left(\text{mmol g}_{cat}^{-1} \text{ h}^{-1}\right) \quad (1)$$

$$r_{CH_4} \text{ (or } r_{CO_2}) = \frac{n_{CH_{4in}} - n_{CH_{4out}} \left(\text{or } n_{CO_{2in}} - n_{CO_{2out}}\right)}{\text{Weight of catayst}}$$
$$\times 60 \text{ (mmol g}_{cat}^{-1} \text{ h}^{-1}) \quad (2)$$

where, $n_{\square} = \dfrac{\text{Flow} \times [\square]}{22.4}$; the signal "$\square$" represents H$_2$, CO, CH$_4$, or CO$_2$.

The reaction selectivity was simplified by eqn (3).

$$\text{Selectivity} = \frac{r_{H_2}}{r_{CO}} \times 100\% \quad (3)$$

The carbon balance rate was estimated by the eqn (4).

$$\text{Carbon balance rate} = \frac{n_{co} + n_{CH_{4out}} + n_{CO_{2out}}}{n_{CH_{4in}} + n_{CO_{2in}}} \times 100\% \quad (4)$$

here, flow is the gas flow rate (mL min^{-1}), and [$\square$] is the respective concentration (vol%) of the corresponding substance detected by online GC.

The energy efficiency of photothermocatalysis was calculated using eqn (5).

$$\eta_{energy} = \frac{\alpha_{CH_4}\left(\text{mol}^{-1}\right)\Delta H_{DRM}{}^0 \left(\text{J mol}^{-1}\right) + \beta\left(\text{mol s}^{-1}\right)\Delta H_{RWGS}{}^0\left(\text{J mol}^{-1}\right)}{\text{light power (J s}^{-1})} \times 100\% \quad (5)$$

rate of 90 mL min^{-1} into the reactor with 5 mg of the samples spread onto a round high pure quartz filter paper (gas hourly space velocity (GHSV) of 1 080 000 mL g$_{cat}^{-1}$ h^{-1}). The catalyst surface temperature was detected by a thermocouple located at the center of the catalyst layer. The products were analyzed by a GC9160 gas chromatograph equipped with an FID and a TCD.

The durability test over Pt/La$_2$O$_3$ and Pt/La$_2$O$_3$–S was performed in the same procedures as the photothermocatalytic activity test, and maintained 200 h or 20 h under focused irradiation with a sample surface temperature of about 700 °C, respectively.

The photocatalytic activity of DRM on Pt/La$_2$O$_3$ was tested using the same stainless-steel reactor at a lower temperature of about 86 °C under irradiation from the Xe lamp. Ice-water bath was used to control the reaction temperature. Also, the other processes were the same as the test of the photothermocatalytic activity.

where, $\alpha_{CH_4} = \dfrac{n_{CH_{4in}} - n_{CH_{4out}}}{3600} \times 10^{-3}$ (mol s^{-1}); $\alpha_{[\square]} = \dfrac{n_{[\square]}}{3600} \times 10^{-3}$(mol s^{-1}); $\beta = \dfrac{\alpha_{CO} - \alpha_{H_2}}{2}$(mol s^{-1}); $\Delta H_{DRM}{}^0$ (247 kJ mol^{-1}); and $\Delta H_{DRM}{}^0$ (41 kJ mol^{-1}) are the standard reaction enthalpy changes of the DRM and RWGS reactions.

3. Results and discussion

3.1 Photothermocatalytic DRM performance

The photothermocatalytic performance of DRM on the catalysts were evaluated under focused irradiation from 300 W Xe lamp without external heating. The mixture gas of CH$_4$/CO$_2$/Ar (8/8/84 vol%) with a flow rate of 90 mL min^{-1} was continuously flowed into a stainless-steel reactor with a quartz window. The photothermocatalytic activity of different samples under a light intensity of 19.42 W cm^{-2} are shown in Fig. 1a and b. For Pt/

16018 | *J. Mater. Chem. A*, 2022, **10**, 16016–16028

This journal is © The Royal Society of Chemistry 2022
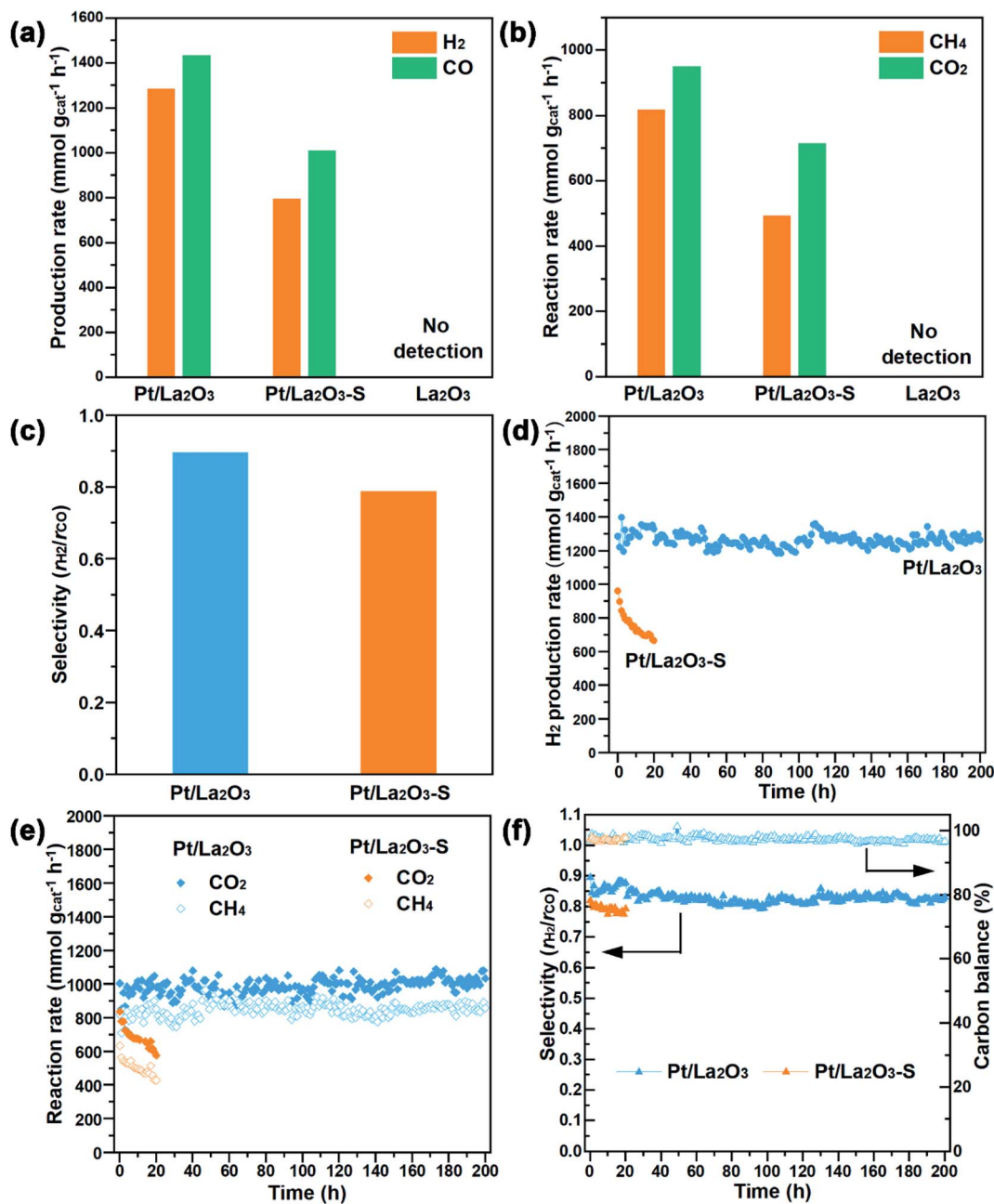
Fig. 1 (a) The production rate of H_2 and CO; (b) the conversion rate of CH_4 and CO_2; (c) the selectivity of Pt/La_2O_3 and Pt/La_2O_3-S; (d–e) the generation rate of H_2 and conversion of reactants during long-term reaction; (f) the selectivity and carbon balance of the samples during durability elevation. Reaction conditions: the samples were under irradiation with a light intensity of 19.42 W cm^{-2} and different sample surface temperature (750 °C on Pt/La_2O_3 and 650 °C Pt/La_2O_3-S) during activity evaluation. For the durability test, the sample surface temperature is 700 °C on Pt/La_2O_3 and Pt/La_2O_3-S with a light intensity of 19.42 W cm^{-2} and 21.69 W cm^{-2}, respectively. For all the experiments, the flow rate of $CH_4/CO_2/Ar$ (8/8/84 vol%) was 90 mL min^{-1}.

La_2O_3-S, the production rate of syngas (r_{H_2} and r_{CO}) is 794.3 and 1009.7 mmol g_{cat}^{-1} h^{-1}, respectively. Pt/La_2O_3 exhibits the highest photothermocatalytic activity with conversion rates of CH_4 (r_{CH_4}) and CO_2 (r_{CO_2}) about 818.7 and 949.9 mmol g_{cat}^{-1} h^{-1}, respectively. Also, high r_{H_2} and r_{CO} values (1284.5 and 1433.6 mmol g_{cat}^{-1} h^{-1}) were monitored on Pt/La_2O_3. The energy efficiency of 8.0% on Pt/La_2O_3 is also higher than that of 5% on Pt/La_2O_3-S. The reactive selectivity expressed by the ratio

of r_{H_2}/r_{CO} is less than 1 (Fig. 1c), which is attributed to the RWGS reaction ($H_2 + CO_2 \rightarrow H_2O + CO$).[22] Pt/La_2O_3 has a relatively higher value of r_{H_2}/r_{CO} compared with Pt/La_2O_3-S. The underlying reason may be that the CO_2 adsorbed on the surface of Pt/La_2O_3 prefers to participate in the oxidation of carbon species (C + CO_2 = 2CO) rather than the hydrogenation of CO_2 ($H_2 + CO_2$ = CO + H_2O). Bare La_2O_3 support exhibits no photothermocatalytic activity, and neither H_2 nor CO are monitored.

The result implies that the Pt NPs or/and interfaces between Pt and La_2O_3 play a crucial role in the efficient activation of CH_4 and CO_2.

Given that carbon deposition or instability of catalysts leads to the deactivation during the DRM reaction, especially at high temperature, the investigation of the tolerance for the catalyst is critical for its practical application.[23,24] The durability tests of photothermocatalytic DRM were performed under light illumination (Fig. 1d–f and S1†). The yield of syngas and the consumption of reaction gas on Pt/La_2O_3–S undergoes a significantly decline (approximately 21%) only after 20 h of reaction, while Pt/La_2O_3 exhibits impressively stable photothermocatalytic ability for at least 200 h with no obvious change in the syngas production and conversion of the reactants. The selectivity is maintained over than 0.80 and the carbon balance is close to 100% on Pt/La_2O_3 (Fig. 1f). Moreover, Pt/La_2O_3 displays considerable production rates of H_2 and CO compared to the reported light-driven DRM on Pt-based catalysts (Table 1). Overall, Pt/La_2O_3 exhibits good photothermocatalytic performance for DRM with a high yield rate of syngas, durability, and stability.

3.2 Characterization of fresh and spent samples

The relevant characterization of Pt/La_2O_3 and Pt/La_2O_3–S was performed to reveal the reason that the photothermocatalytic DRM efficiently proceeds on Pt/La_2O_3 (Pt/La_2O_3–U and Pt/La_2O_3–S–U labeled as the used samples). Considering Pt species as the main active components for all Pt-doped samples, the form of Pt species was observed by HRTEM (Fig. 2a–d). The distinct lattice spacing value with 1.97 or 2.27 nm is attributed to the (100) or (111) facets of Pt species, respectively. Pt NPs with an average size approaching 2 nm are dispersed on La_2O_3 of both Pt/La_2O_3 and Pt/La_2O_3–S, as shown in the HRTEM images (Fig. 2a and b). Compared to the fresh Pt/La_2O_3, Pt NPs on spent Pt/La_2O_3 still exists with a size of approximately 2 nm without obvious aggregation (Fig. 2c). Elemental mapping (Fig. 2e and f) shows that Pt NPs are still highly dispersed on spent Pt/La_2O_3 such as the fresh catalyst. At the same time, no carbon rings,

fibers, or filaments are found on spent Pt/La_2O_3. The HRTEM image of used Pt/La_2O_3–S (Fig. 2d) displays enlarged Pt NPs with a mean diameter of 4.40 nm and even a portion of particles with size larger than 5 nm according to Pt NPs' aggregation after the reaction. Furthermore, significant carbon deposition can be observed on Pt/La_2O_3–S–U (Fig. S2†). TGA was used to check the coking on the spent catalyst (Fig. S3†). No mass loss was observed in used Pt/La_2O_3, indicating that no carbon deposition occurred. Also, only a slight increase occurs in the mass curve due to oxygen filling on the oxygen vacancies.[29] The oxygen vacancies play a key role in achieving high DRM performance by participating in the DRM reaction and eliminating the carbon species.[27] In contrast, spent Pt/La_2O_3–S shows a significant mass reduction peak near 600 °C, which belongs to the oxidation of carbon species on the catalyst. Carbon deposition can cover the catalytic active sites and reduce the catalytic activity of the catalyst, which is detrimental to the catalytic stability of the catalyst.[22] Therefore, Pt/La_2O_3 exhibits higher photothermocatalytic activity and better resistance to the sintering of Pt NPs and coking during DRM.

To further reveal the underlying reasons of differences in stability and coke-resistance of the samples, XRD was subsequently performed. The typical characteristic peaks of La_2O_3 (JCPDF No. 01-083-1344) are observed on all the Pt NPs supported samples but no Pt characteristic peak is found from the XRD patterns (Fig. 3a), implying that Pt NPs are possibly small sized and are highly dispersed on the support. The results are consistent with the HRTEM results. After the reaction, the characteristic diffraction peaks of $La_2O_2CO_3$ (JCPDF No. 01-084-1963) appear in the light blue region of Fig. 3a over Pt/La_2O_3–U and Pt/La_2O_3–S–U, according to the reaction of La_2O_3 and CO_2 to produce intermediate $La_2O_2CO_3$ (La_2O_3 + CO_2 = $La_2O_2CO_3$).[30,31] XPS was performed to evaluate the variation in valence and chemical interaction. The XPS spectra of Pt show that the peak of Pt^0 on Pt/La_2O_3 appears at a higher B.E. after the reaction is ascribed to the reduction in the electron density, which indicates the formation of strong interaction between the metal and the support during the reaction (Fig. 3b).[32] Moreover, Pt species on Pt/La_2O_3 before and after the DRM reaction are

Table 1 Comparison of the catalytic performance on the reported Pt-based catalyst for DRM under light irradiation with the results in this work

| Catalyst | Temperature (°C) with or without external heating | Production (mmol g^{-1} h^{-1}) | | Selectivity (r_{H_2}/r_{CO}) | Stability | Ref. |
		H_2	CO			
Pt/La_2O_3	500	290.0	406.8	0.71	Stable during 200 h at 700 °C	This work
	600	624.8	805.8	0.78		
	700	1284.5	1433.7	0.89		
Pt/CeO_2–MNR	767	342.0	360.0	0.95	Slightly deactivation during 100 h at 767 °C	13
Pt–Au/SiO_2	400 with heating	6.0	7.2	0.83	Little deactivation during 6 h at 400 °C	11
Pt/TaN	500 with heating	66.0	72.0	0.92	Oblivious deactivation over 5 h at 500 °C	10
$Pt/black\ TiO_2$	550 with heating	71.0	158.0	0.45	Deactivation during 30 h at 600 °C	9
	650 with heating	129.0	370.0	0.35		
$MgO/Pt/Zn$–CeO_2	600 with heating	356.0	516.0	0.69	Stable during 20 h at 600 °C	25
Pt–Si–CeO_2	600 with heating	90.0	154.0	0.58	Decline before first 5 h during 30 h at 600 °C	26
Pt/Al_2O_3–CeO_2	700 with heating	657	666	0.99	Stable during 10 h at 700 °C	27
$Pt/mesoporous$–TiO_2	500 with heating	178.6	281.0	0.64	Slightly deactivation during 10 h at 500 °C	28

16020 | *J. Mater. Chem. A*, 2022, **10**, 16016–16028

This journal is © The Royal Society of Chemistry 2022
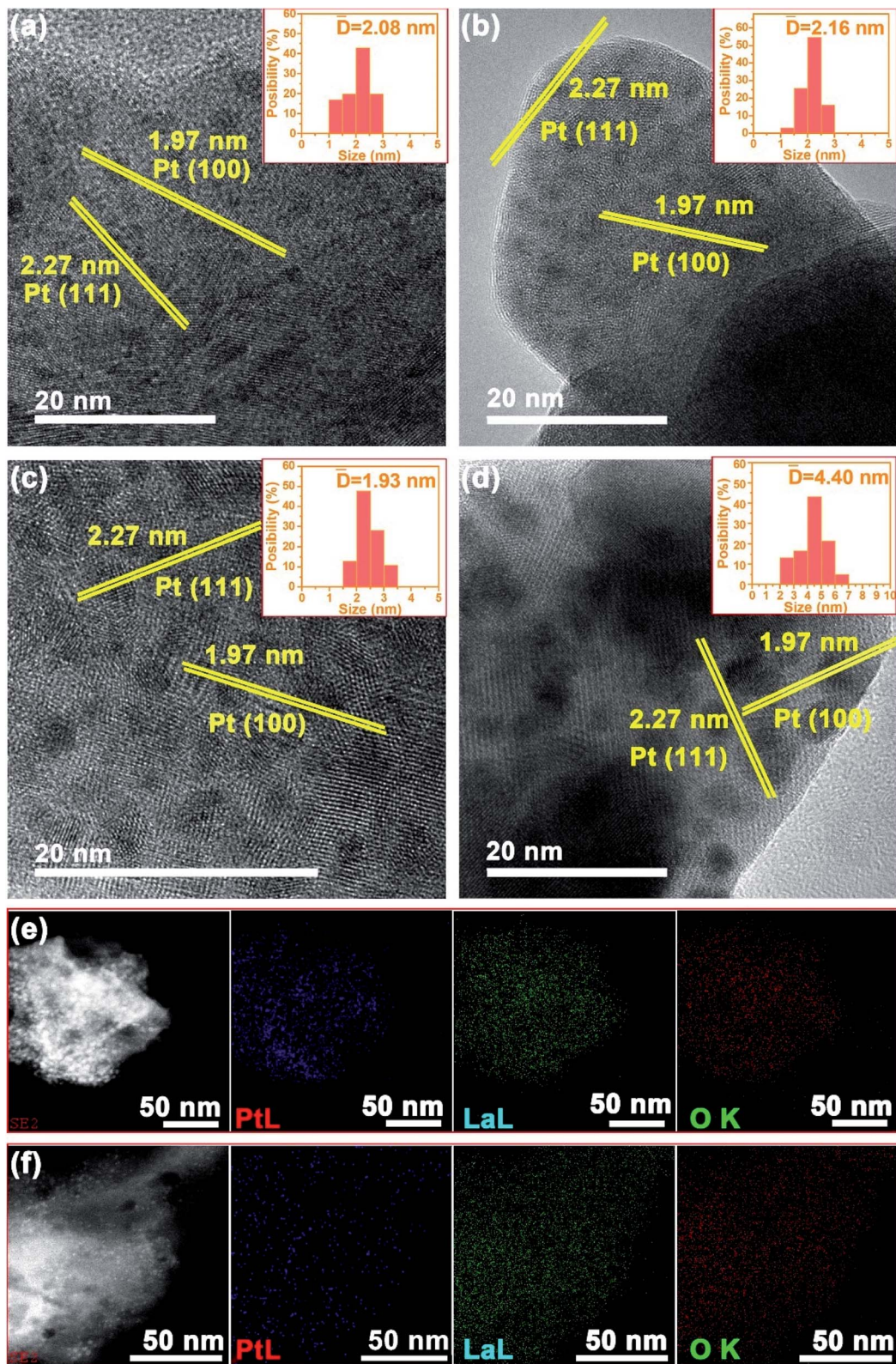
Fig. 2 (a–d) HRTEM images of Pt/La_2O_3, Pt/La_2O_3–S, Pt/La_2O_3–U, and Pt/La_2O_3–S–U, and the distribution of the particle size in the inset. Element mapping of (e) Pt/La_2O_3 and (f) Pt/La_2O_3–U.

mainly in the form of the metal state (Pt^0) and the proportion of Pt^0 shows no obvious fluctuation, which also proves that the formed strong interaction between Pt and the support makes Pt

NPs extremely stable. Compared with fresh Pt/La_2O_3–S, Pt species on spent Pt/La_2O_3–S tend to convert into Pt^0, and the ratio of Pt^0 changes from 0.38 to 0.64, which is closed to the

This journal is © The Royal Society of Chemistry 2022

J. Mater. Chem. A, 2022, 10, 16016–16028 | 16021
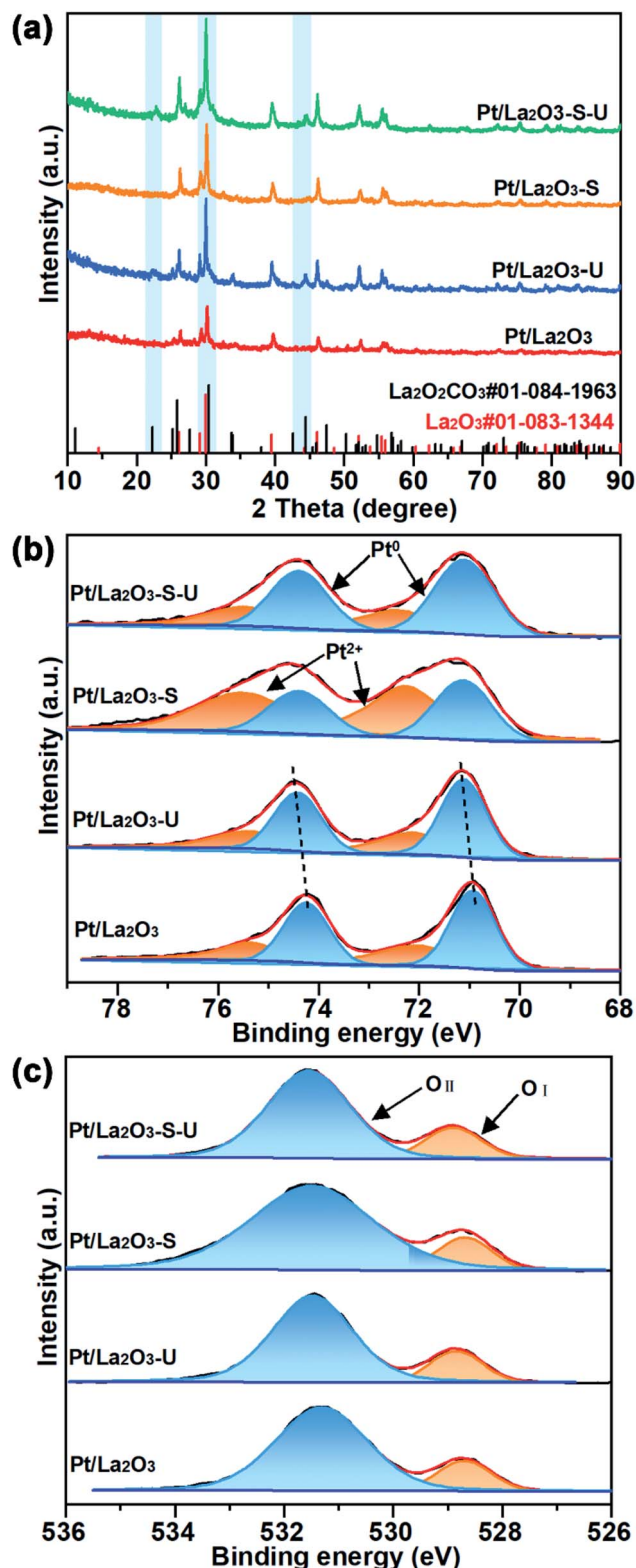
Fig. 3 (a) XRD patterns; (b) XPS spectra of Pt 4f; (c) XPS spectra of O 1s.

ratio of Pt^0 on Pt/La_2O_3; however, the catalytic performance of Pt/La_2O_3–S–U is far less than that of Pt/La_2O_3–S. The results indicate that the valence of Pt in the samples does not play a major role in the catalytic performance and Pt NPs are

unstable (Fig. 3b and Table S1†), which is consistent with the HRTEM results on the stabilization of Pt NPs on Pt/La_2O_3 and the sintering of Pt NPs occurred on Pt/La_2O_3–S. Considering that oxygen vacancy contributes to coke-resistance, the O 1s XPS spectrum was also recorded to further compare the oxygen vacancy concentrations. The lattice oxygen (O_I) with low B.E. (~528.8 eV) and surface oxygen with low coordination (O_{II}) at high B.E. (~531.5 eV) are identified in Fig. 3c.[33] Surface adsorbed oxygen species, such as defect-oxide O^{2-} or O^-, readily form in the presence of unsaturated oxygen.[34] The proportion of O_{II} in used Pt/La_2O_3–S decreases, while it hardly changes in Pt/La_2O_3 after the reaction (Fig. 3c and Table S1†), which indicates more and stable oxygen vacancies on Pt/La_2O_3. From the EPR spectra (Fig. S4†), the signal at $g = 2.003$ belongs to oxygen vacancies. The result shows that Pt doping induces more oxygen vacancy generation, and Pt/La_2O_3 exhibits more oxygen vacancies than Pt/La_2O_3–S, which contributes to the excellent resistance of deposited carbon on Pt/La_2O_3.[35–37] As described above, the synergistic effect of strong interaction between Pt and La_2O_3 and oxygen vacancies makes Pt/La_2O_3 show better photothermocatalytic durability during the DRM reaction.

3.3 The role of light: heating and light promotion

To investigate the role of light in photothermocatalysis, the optical properties were firstly detected by DRS, as shown in Fig. 4a. Compared with La_2O_3, Pt loading can significantly broaden and enhance the intensity of the absorption peak on the samples, which is attributed to the LSPR of Pt NPs.[38] Strong absorption induces thermal energy by generating more energetic hot electrons, resulting in high surface temperature with a temperature value of 700 and 650 °C for Pt/La_2O_3 and Pt/La_2O_3–S, respectively (Fig. S5†). Furthermore, the absorbance intensity of Pt/La_2O_3 exhibits distinct enhancement from 200 nm to 1800 nm, which is ascribed to the strong interaction between Pt and La_2O_3, which contributes to long-term durability and promotes the reaction activity.

Pt/La_2O_3 achieved highly-efficient photothermocatalytic activity. To determine the effect of traditional photocatalysis, the low-temperature experiment under irradiation was conducted by controlling the reaction temperature at 86 °C. No H_2 and CO were detected (Fig. S6†), which manifests that Pt/La_2O_3 exhibits inert photocatalytic activity. The low activity of Pt/La_2O_3 under UV-vis irradiation with surface temperature of 252 °C also confirms that the role of photogenerated charge carriers in the traditional photocatalytic process is negligible during the reaction process (Table 2). From Table 2, H_2 and CO are not generated on Pt/La_2O_3 under infrared radiation at 125 °C, but the value of r_{H_2} and r_{CO} increases under UV-visible at 365 °C compared with that at 252 °C, indicating that photogenerated charge carrier recombined by a nonradiative recombination process leads to photothermal conversion to improve the catalytic activity. Infrared light (IR)-induced heating effect from the full spectrum contributes to the elevation of the surface temperature from 365 to 500 °C, and the yield of syngas is dramatically enhanced, which similarly discloses that the temperature increase has a positive effect on the

16022 | J. Mater. Chem. A, 2022, 10, 16016–16028

This journal is © The Royal Society of Chemistry 2022
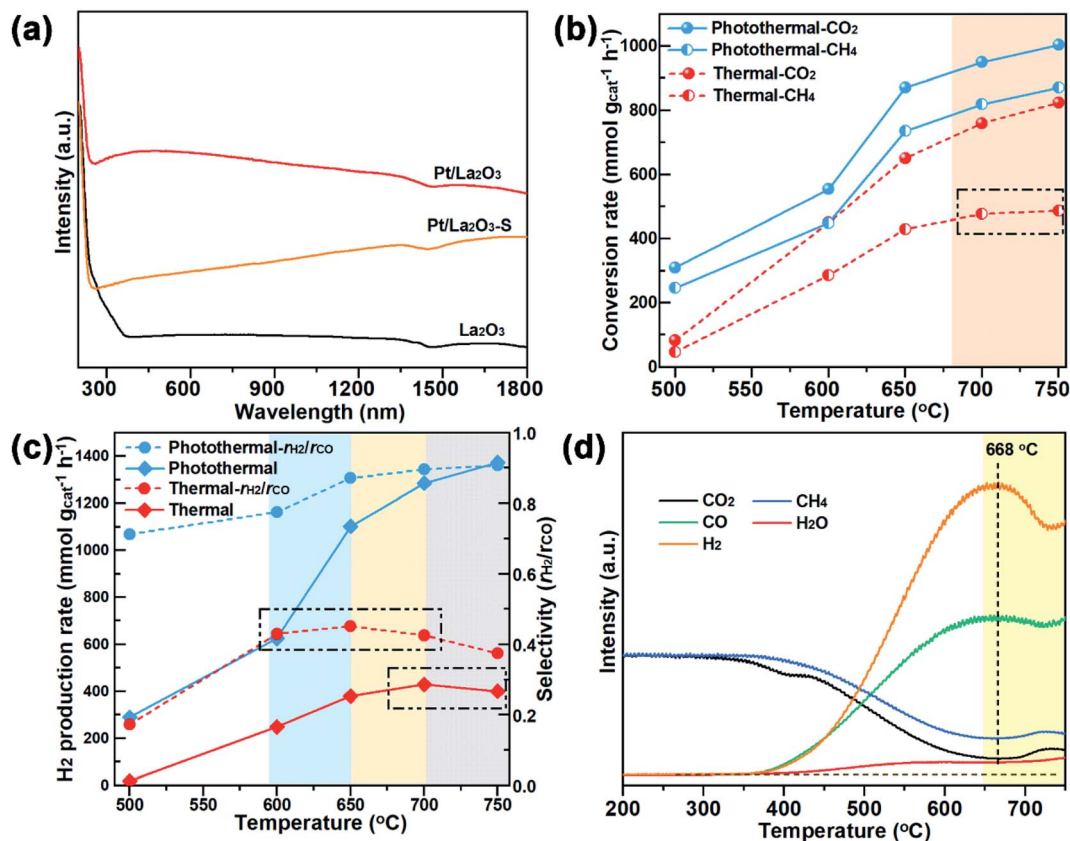
Fig. 4 (a) DRS spectra of La_2O_3, Pt/La_2O_3-S, and Pt/La_2O_3; (b) the CH_4 and CO_2 conversion rate of Pt/La_2O_3 under irradiation or in dark; (c) the H_2 yield rate and selectivity of Pt/La_2O_3 under irradiation or in dark; (d) CH_4/CO_2^-TPSR date for the MS signal on Pt/La_2O_3.

Table 2 Catalytic performance of Pt/La_2O_3 under different light irradiation

Treatment	Light intensity (W cm^{-2}) and surface temperature of catalyst layer (°C)	Production (mmol g^{-1} h^{-1})		Selectivity (r_{H_2}/r_{CO})
		H_2	CO	
UV-vis-IR[a]	12.9, 500	289.9	406.8	0.71
UV-vis[a]	7.4, 370	28.0	48.1	0.58
UV-vis[a]	7.4, 252[b]	1.3	4.1	0.32
IR[a]	1.5, 125	0	0	-

[a] Irradiation was conducted using 300 W Xe Lamp. [b] Sample surface temperature was controlled by an ice-water bath.

photothermocatalytic activity of DRM. Furthermore, in order to illustrate the influence of thermal energy in the photothermocatalytic activity, the activity of thermocatalysis induced by additional heating and photothermocatalysis under irradiation were compared at the same surface temperature. During thermocatalysis, the consumption of CO_2 increases as the temperature increases from 500 to 750 °C, and the value of r_{CH_4} firstly enhances and subsequently stabilizes, after which the temperature reaches 700 °C (Fig. 4b). The r_{H_2} value increases when the reaction temperature is below 700 °C, and then decreases with increasing temperature (Fig. 4c). The reaction selectivity shows the same trend with r_{H_2} and reaches a maximum value of ~0.45 at 650 °C. The competition reaction of H_2 with CO_2 leads to the reduction of selectivity and

continuous enhancement of r_{CO_2} at high temperature in thermocatalysis. Moreover, CH_4/CO_2-TPSR was operated to monitor the side reactions and further the analyze thermocatalytic performance (Fig. 4d). The reaction is triggered with a reduced signal in CH_4 and CO_2 at about 400 °C, and H_2, CO, and H_2O are produced. In addition, H_2O (except for the reactants, CO and H_2), is the only substance detected during the reaction, and the signal intensity gradually rises with the increase in temperature, indicating that the RWGS reaction is the main side reaction in DRM. The signal intensity of H_2 achieves its maximum value at about 668 °C and then starts to decrease significantly, while the signal intensity of CO is slightly changed. Considering the above results comprehensively, the RWGS reaction is more obvious when the temperature exceeds ~668 °C, resulting in the

consumption of more H_2 to generate more H_2O and CO. The results indicate that high temperature promotes the RWGS reaction in thermocatalysis. The photothermocatalytic performance under light irradiation without additional heating increases with enhanced light intensity accompanying the sample surface temperature increase. External heating induces high surface temperature in thermocatalysis, and the temperature is very uniform in all the samples. However, the surface temperature distribution of Pt/La_2O_3 is different in photothermocatalytsis (Fig. S7†). When the maximum temperature reaches 700 °C at the center of Pt/La_2O_3, the temperature value on the sample edge is only approximately 500 °C. All the results indicate that the photothermocatalytic activity is significantly better than those of thermocatalysis at different temperatures. The r_{H_2} value is approximately 16.0 or 3.0 times than that of thermocatalysis at 500 and 700 °C, respectively. At 500 °C or 750 °C, the selectively under light irradiation improves to ~4.1 or 2.1 times than that of thermocatalysis, respectively. In addition, the selectivity of photothermocatalysis continues to increase with temperature above 650 °C, which is quite different from thermocatalysis, indicating that light can facilitate CO_2 reduction by CH_4 rather than by H_2. These results suggest that the effect of photoactivation causes the enhancement of the photothermocatalytic activity compared to thermocatalysis.

The adsorption ability of the reactants on the catalyst has an important effect on the reaction, and the adsorption of gas molecules can be affected by the photothermal effect.[39,40] Therefore, CH_4-TPD and CO_2-TPD were performed under light irradiation or in dark to determine the effect of light; the results are depicted in Fig. 5a and b. Pt/La_2O_3 under illumination displays enhanced desorption amount of CH_4 and CO_2 than that in dark, which indicates the better adsorption and activation abilities for CH_4 and CO_2 on Pt/La_2O_3 with light. Generally, the studies consider the DRM reaction starting with the cleavage of C–O bonds in CO_2 and C–H bonds in CH_4, respectively. Then, the intermediate surface reaction derived from the activation of the reactant forms products, and the final products are desorbed. The disassociation of C–H bonds in the methane molecule is the rate-determining step of the DRM.[31] CH_4-TPSR and CO_2-TPSR were operated on Pt/La_2O_3 under irradiation or in dark to elucidate why light irradiation played a crucial role in augmenting the catalytic activity and selectivity (Fig. 5c and d). The detected H_2 signal is sufficient to certify the decomposition of CH_4 (Fig. 5c). CH_4 dehydrogenation begins at approximately 315 °C and 341 °C under light irradiation and in dark, respectively. Lower temperature under light irradiation reveals that light accelerates the activation of CH_4 (a slight decrease in CH_4 makes the CH_4 signal unremarkable due to the high concentration of CH_4 being introduced during the experiment). In addition, the monitored CO signal subjected to the production of CO discloses that the oxygen species on the catalyst takes part in the reaction, which contributes to the oxidation of C* species dissociated from CH_4, thus further preventing coking. CO starts to be produced at about 398 °C or 408 °C under illumination and dark conidiation, respectively. Carbonaceous species over the sample under light irradiation are more rapidly and easily formed than CO, which is mainly because light irradiation

promotes the desorption of surface oxygen atoms by weakening the metal–oxygen bond.[41] The result also proves that light accelerates the further reaction of dissociated CH_4 on Pt/La_2O_3. The consumption peak of CO_2 preferentially appears at ~334 °C under light irradiation during CO_2-TPSR, which is significantly lower than that in dark (399 °C) (Fig. 5d). All the TPSR results are in line with the results of CH_4-TPD and CO_2-TPD. Oxygen vacancies have been reported to play a crucial role in CO_2 activation. EPR analysis was conducted under light irradiation and in dark (Fig. 5e) to verify the oxygen vacancies and the formation of free electrons without coupling. The signal at $g = 2.003$ on Pt/La_2O_3 under light irradiation is stronger than that in dark, indicating the generation of more oxygen vacancies on the catalyst and the formation of more free radicals trapped on surface oxygen-vacancy sites under light irradiation, which is ascribed to electron transfer according to LSPR of Pt NPs.[35,42] Also, the electrons can further transfer to adsorbates and facilitate CO_2 activation to promote the production of syngas, which is in accordance with the DRS result.[11] The superior CO_2 dissociation ability under light conditions also accelerates the removal of carbonaceous species due to the oxidation of carbon species to CO by O* dissociated from CO_2 and suppresses coke deposition.

The adsorption–desorption capacity of the products on the catalyst surface determines the reaction rate. To further elucidate light-effective promotion reaction rate and selectivity, CO-TPD and H_2-TPD on Pt/La_2O_3 in dark or under light irradiation have been investigated. The desorption ability of CO on the sample shows little difference between light and dark conditions (Fig. S8†). The adsorption ability of Pt/La_2O_3 for H_2 in dark is much higher than that under light irradiation (Fig. 5f). The poor H_2 adsorption performance under light reveals that light-excited hot electrons contribute to the removal of H_2 from the catalyst surface and further accelerate the reaction of DRM.[3,43] The rapid desorption of H_2 with light suppresses the reaction between adsorbed H and O, contributing to higher selectivity and stability of photothermocatalysis and endowing higher abundance of mobile O that can the scavenge C species, which is in accordance with the above experimental results.

The intermediate species during DRM on Pt/La_2O_3 in dark or under light irradiation at 400 °C was observed through *in situ* DRIFTS (Fig. 6a). As the temperature increases, the conversion of CH_4 and CO_2 is manifested in the gradual weakening of the absorption peaks of CH_4 (3016 cm^{-1} and 1302 cm^{-1}) and CO_2 (2360 cm^{-1} and 2340 cm^{-1}).[44] The broad peaks at *ca.* 1440 cm^{-1} and 835 cm^{-1} are assigned to $La_2O_2CO_3$ formed by La_2O_3 and CO_2 with increasing temperature, which are in good agreement with the XRD results.[45,46] In addition, the formation of $La_2O_2CO_3$ facilitates the elimination of carbon species from the metal surface.[31] The symmetric and asymmetric deformation vibrations of adsorbed –CH_3 groups present at *ca.* 1354 cm^{-1} or 1341 cm^{-1} after CH_4 and CO_2 are introduced, showing that CH_4 is dissociated into –CH_3 and H species.[44] Related studies have proved that the generation or activation of –CH_3 can be achieved at room temperature, which is consistent with the abovementioned result.[47,48] When the temperature is increased to 400 °C and maintained for 30 min, the intensity of the

16024 | *J. Mater. Chem. A*, 2022, **10**, 16016–16028

This journal is © The Royal Society of Chemistry 2022
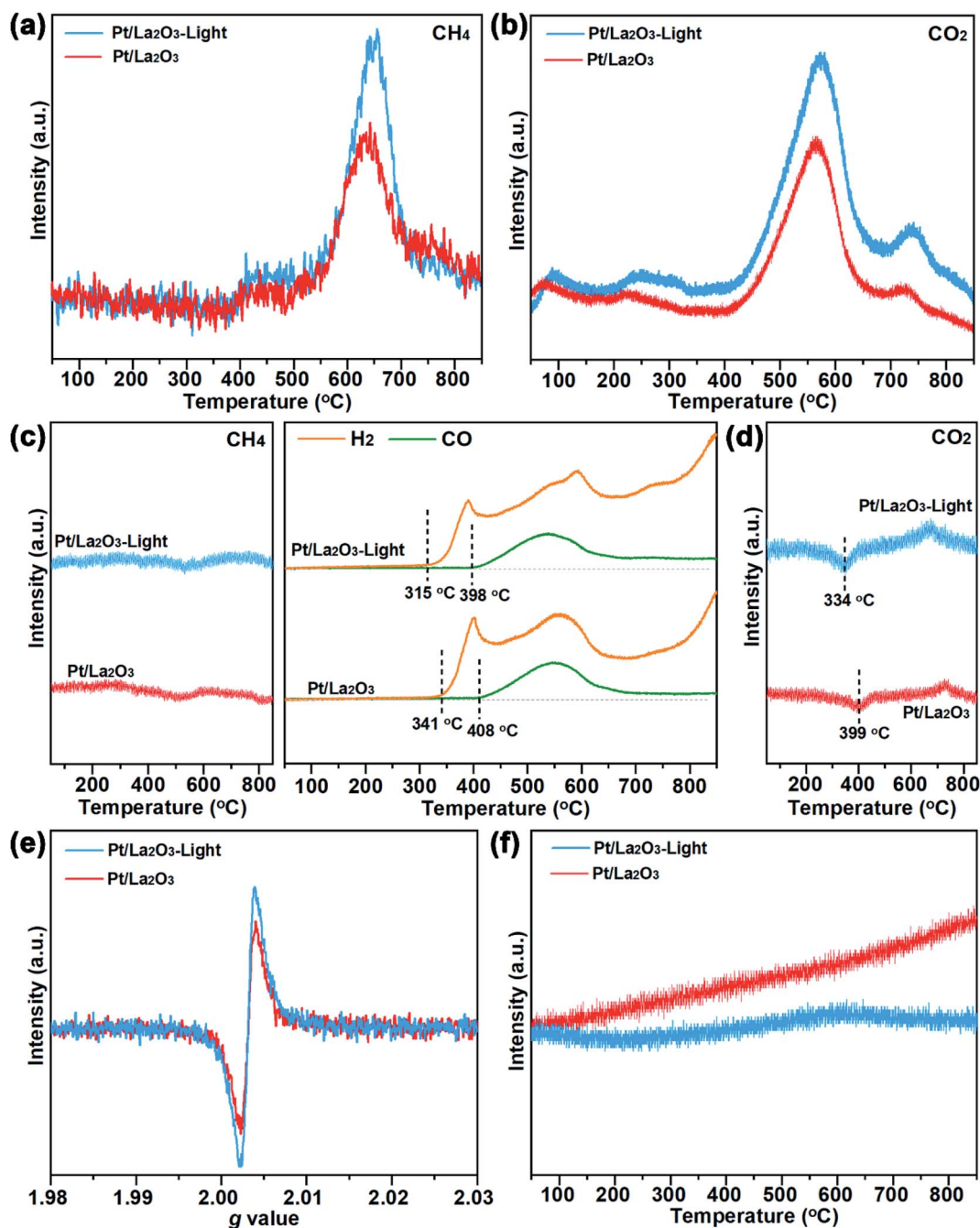
Fig. 5 (a) CH_4-TPD and (b) CO_2-TPD of the MS signal for Pt/La_2O_3 with or without light illumination; (c) CH_4-TPSR of the MS signal for Pt/La_2O_3 with or without light illumination; (d) CO_2-TPSR of the MS signal for Pt/La_2O_3 with or without light illumination; (e) EPR spectra of Pt/La_2O_3 under irradiation or in dark; (f) H_2 desorption of the MS signal for Pt/La_2O_3 in dark or light.

absorption peak of methyl groups under light is significantly reduced than that in dark, indicating that light promotes the cracking of the methyl group. New broad bands at *ca.* 1046 cm^{-1} corresponding to C–O stretching appears at 400 °C under light irradiation but does not appear until the temperature at 400 °C is maintained for 30 min without light.[13] The observation is ascribed to the dissociation of CH_4 on Pt NPs and the reaction with adsorbed oxygen to form the C–O species, which is consistent with the CH_4-TPSR results.[13] At the same time, the LSPR of Pt NPs excites a large number of hot electrons under the

irradiation of light, which benefits to accelerate the activation and dissociation of CH_4.[11] When the temperature is increased to 400 °C under light irradiation, an enhanced absorption peak appears at *ca.* 1180 cm^{-1}, which is attributed to the C–O species dissociated from CO_2 on the site of oxygen vacancy.[13] The peak is particularly weak in dark conditions, which is consistent with the CO_2-TPSR results. Furthermore, the dissociation of CO_2 is also evidenced through the formation of bidentate formate (1580 cm^{-1}), which can transform to the final CO or H_2O.[49] The intensity of the peak under light is lower than that in dark due

This journal is © The Royal Society of Chemistry 2022

J. Mater. Chem. A, 2022, **10**, 16016–16028 | **16025**
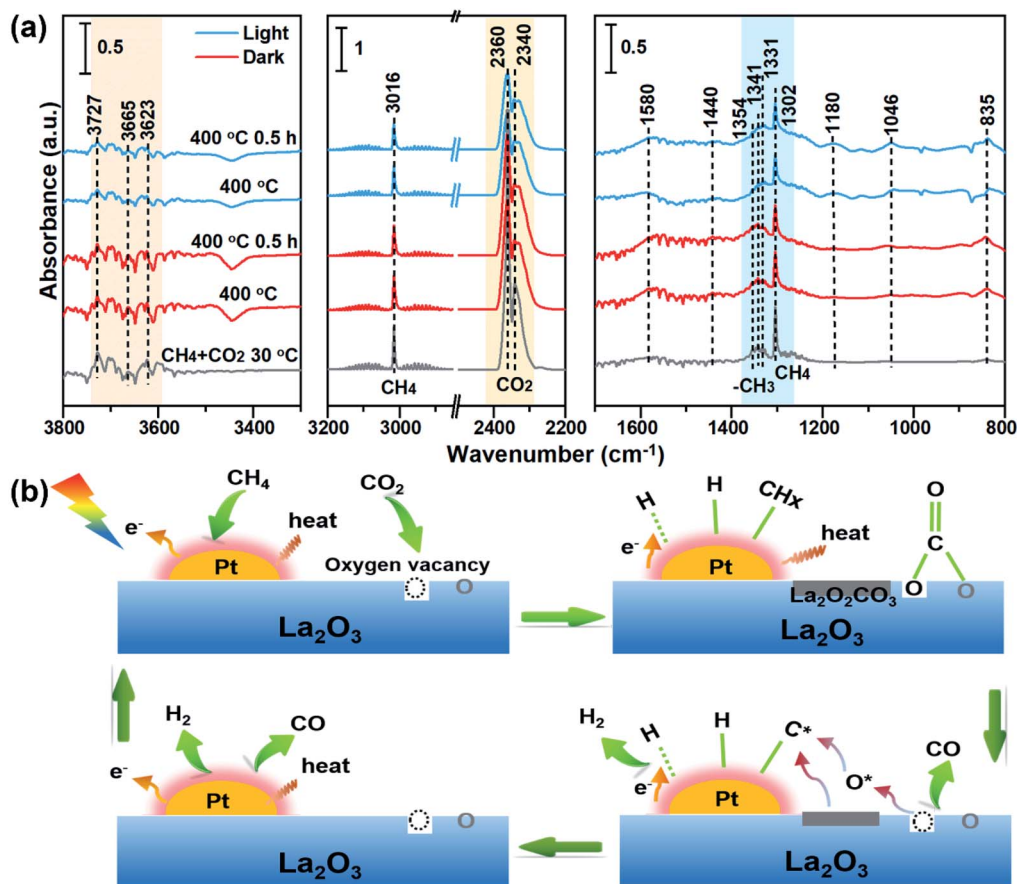
Fig. 6 (a) *In situ* DRIFTS of Pt/La$_2$O$_3$ during DRM at 400 °C in dark and under irradiation; (b) reaction mechanism of photothermocatalytic DRM on Pt/La$_2$O$_3$.

to which light facilitates the dissociation of intermediates. In addition, the adsorbed hydroxyl groups of H$_2$O involving the RWGS reaction were observed at *ca.* 3500–3750 cm^{-1}, and the intensity of these peaks is weaker under light than that in dark, indicating that light restrains H$_2$O production and improves the reaction selectivity.[44]

In view of the above results, a possible reaction mechanism is described in Fig. 6b. Under light irradiation, LSPR on Pt/La$_2$O$_3$ excites more number of hot electrons and oxygen vacancies and initiates the surface temperature of the catalyst, which promotes the reaction through the following processes. CH$_4$ dissociation is converted to CH$_x$ and H$^+$, which is further transformed to C* and H$_2$. The light-excited hot electrons also promote the spontaneous desorption of H$_2$. CO$_2$ dissociates to form CO, O*, or formate intermediates. In addition, CO$_2$ can react with La$_2$O$_3$ to form La$_2$O$_2$CO$_3$. O* and La$_2$O$_2$CO$_3$ facilitate C* oxidation to CO. The synergy of photothermal reaction and photoactivation is the key in the photothermocatalytic DRM process.

4. Conclusion

In this study, stable and highly dispersed Pt NPs was supported on La$_2$O$_3$ (Pt/La$_2$O$_3$) for highly-efficient photothermocatalytic DRM. The selectivity (>0.80) and the production rate of H$_2$ on Pt/

La$_2$O$_3$ are not reduced during the 200 h reaction at 700 °C. The synergistic effects of strong Pt-support interaction and oxygen vacancies lead to the good stability of Pt NPs and coke-resistance on Pt/La$_2$O$_3$. The value of r_{H_2} and selectivity during photothermocatalysis is up to 3.0 or 2.1 times of those in thermocatalysis when the sample surface temperature is about 700 °C. All the results of *in situ* DRIFTS, H$_2$-TPD, CH$_4$-TPSR, and CO$_2$-TPSR reveal that more oxygen vacancies and hot electrons excited by light illumination accelerate the activation and the further dissociation of CH$_4$ and CO$_2$. In addition, the spontaneous desorption of H$_2$ formed under light illumination suppresses RWGS reaction and further improves the catalytic activity and selectivity. The results will be conducive for the construction of an efficient and tolerable photothermocatalyst for DRM, and provide a strategy for the efficient utilization of CH$_4$ and CO$_2$ as energy storage resources.

Conflicts of interest

The authors declare no competing financial interest.

Acknowledgements

16026 | *J. Mater. Chem. A*, 2022, **10**, 16016–16028

This journal is © The Royal Society of Chemistry 2022

References

1 L. Azancot, L. F. Bobadilla, M. A. Centeno and J. A. Odriozola, *Appl. Catal., B*, 2021, **285**, 119822.

2 Y. Song, E. Ozdemir, S. Ramesh, A. Adishev, S. Subramanian, A. Harale, M. Albuali, B. A. Fadhel, A. Jamal, D. Moon, S. H. Choi and C. T. Yavuz, *Science*, 2020, **367**, 777–781.

3 L. Zhou, J. M. P. Martirez, J. Finzel, C. Zhang, D. F. Swearer, S. Tian, H. Robatjazi, M. Lou, L. Dong, L. Henderson, P. Christopher, E. A. Carter, P. Nordlander and N. Halas, *Nat. Energy*, 2020, **5**, 61–70.

4 S. Wu, Y. Li, Q. Zhang, Z. Jiang, Y. Yang, J. Wu and X. Zhao, *Energy Environ. Sci.*, 2019, **12**, 2581–2590.

5 Q. Zhang, M. Mao, Y. Li, Y. Yang, H. Huang, Z. Jiang, Q. Hu, S. Wu and X. Zhao, *Appl. Catal., B*, 2018, **239**, 555–564.

6 Z. Wang, X. M. Cao, J. Zhu and P. Hu, *J. Catal.*, 2014, **311**, 469–480.

7 V. Pawar, D. Ray, C. Subrahmanyam and V. M. Janardhanan, *Energy Fuels*, 2015, **29**, 8047–8052.

8 S. Wu, Y. Li, Q. Hu, J. Wu and Q. Zhang, *ACS Sustainable Chem. Eng.*, 2021, **9**, 11635–11651.

9 B. Han, W. Wei, L. Chang, P. Cheng and Y. H. Hu, *ACS Catal.*, 2015, **6**, 494–497.

10 H. Liu, H. Song, W. Zhou, X. Meng and J. Ye, *Angew. Chem., Int. Ed. Engl.*, 2018, **57**, 16781–16784.

11 H. Song, X. Meng, T. D. Dao, W. Zhou, H. Liu, L. Shi, H. Zhang, T. Nagao, T. Kako and J. Ye, *ACS Appl. Mater. Interfaces*, 2018, **10**, 408–416.

12 X. Meng, T. Wang, L. Liu, S. Ouyang, P. Li, H. Hu, T. Kako, H. Iwai, A. Tanaka and J. Ye, *Angew. Chem., Int. Ed. Engl.*, 2014, **53**, 11478–11482.

13 M. Mao, Q. Zhang, Y. Yang, Y. Li, H. Huang, Z. Jiang, Q. Hu and X. Zhao, *Green Chem.*, 2018, **20**, 2857–2869.

14 T. W. Hansen, A. T. Delariva, S. R. Challa and A. K. Datye, *Acc. Chem. Res.*, 2013, **46**, 1720–1730.

15 Y. Tang, Y. Wei, Z. Wang, S. Zhang, Y. Li, L. Nguyen, Y. Li, Y. Zhou, W. Shen, F. F. Tao and P. Hu, *J. Am. Chem. Soc.*, 2019, **141**, 7283–7293.

16 S. Liu, H. Qi, J. Zhou, W. Xu, Y. Niu, B. Zhang, Y. Zhao, W. Liu, Z. Ao, Z. Kuang, L. Li, M. Wang and J. Wang, *ACS Catal.*, 2021, **11**, 6081–6090.

17 J. Dong, Q. Fu, H. Li, J. Xiao, B. Yang, B. Zhang, Y. Bai, T. Song, R. Zhang, L. Gao, J. Cai, H. Zhang, Z. Liu and X. Bao, *J. Am. Chem. Soc.*, 2020, **142**, 17167–17174.

18 J. Li, Y. Lin, X. Pan, D. Miao, D. Ding, Y. Cui, J. Dong and X. Bao, *ACS Catal.*, 2019, **9**, 6342–6348.

19 H. Chen, S. Z. Yang, Z. Yang, W. Lin, H. Xu, Q. Wan, X. Suo, T. Wang, D. E. Jiang, J. Fu and S. Dai, *ACS Cent. Sci.*, 2020, **6**, 1617–1627.

20 H. Xin, L. Lin, R. Li, D. Li, T. Song, R. Mu, Q. Fu and X. Bao, *J. Am. Chem. Soc.*, 2022, **144**(11), 4874–4882.

21 G. Lu, S. Z. Li, Z. Guo, O. K. Farha, B. G. Hauser, X. Y. Qi, Y. Wang, X. Wang, S. Y. Han, X. G. Liu, J. S. DuChene, H. Zhang, Q. C. Zhang, X. D. Chen, J. Ma, S. C. J. Loo, W. D. Wei, Y. H. Yang, J. T. Hupp and F. W. Huo, *Nat. Chem.*, 2012, **4**, 310–316.

22 X. Liu, H. Shi, X. Meng, C. Sun, K. Zhang, L. Gao, Y. Ma, Z. Mu, Y. Ling, B. Cheng, Y. Li, Y. Xuan and Y. Ding, *Sol. RRL.*, 2021, 5.

23 L. Wang, L. Wang, X. Meng and F. S. Xiao, *Adv. Mater.*, 2019, 1901905.

24 M. Akri, S. Zhao, X. Li, K. Zang, A. F. Lee, M. A. Isaacs, W. Xi, Y. Gangarajula, J. Luo, Y. Ren, Y. T. Cui, L. Li, Y. Su, X. Pan, W. Wen, Y. Pan, K. Wilson, L. Li, B. Qiao, H. Ishii, *et al.*, *Nat. Commun.*, 2019, **10**, 5181.

25 F. Pan, X. Xiang, Z. Du, E. Sarnello, T. Li and Y. Li, *Appl. Catal., B*, 2020, **260**, 118189.

26 F. Pan, X. Xiang, W. Deng, H. Zhao, X. Feng and Y. Li, *ChemCatChem*, 2017, **10**, 940–945.

27 X. Feng, Z. Du, E. Sarnello, W. Deng, C. R. Petru, L. Fang, T. Li and Y. Li, *J. Mater. Chem. A*, 2022, **10**, 7896–7910.

28 Z.-Y. Zhang, T. Zhang, W.-P. Liang, P.-W. Bai, H.-Y. Zheng, Y. Lei, Z. Hu and T. Xie, *Energy Convers. Manage.*, 2022, 258.

29 Y. Huang, K. Li, S. Li, Y. Lin, H. Liu and Y. Tong, *ChemistrySelect*, 2018, **3**, 7423–7428.

30 N. Bonmassar, M. F. Bekheet, L. Schlicker, A. Gili, A. Gurlo, A. Doran, Y. Gao, M. Heggen, J. Bernardi, B. Klötzer and S. Penner, *ACS Catal.*, 2020, **10**, 1102–1112.

31 V. S. Sandoval-Bohórquez, E. M. Morales-Valencia, C. O. Castillo-Araiza, L. M. Ballesteros-Rueda and V. G. Baldovino-Medrano, *ACS Catal.*, 2021, **11**, 11478–11493.

32 J. Chen, X. Lv, W. Xu, X. Li, J. Chen and H. Jia, *Appl. Catal., B*, 2021, 290.

33 C. V. Ramana, R. S. Vemuri, V. V. Kaichev, V. A. Kochubey, A. A. Saraev and V. V. Atuchin, *ACS Appl. Mater. Interfaces*, 2011, **3**, 4370–4373.

34 H. Wang, W. Yang, K. Bian, W. Zeng, X. Jin, R. Ouyang, Y. Xu, C. Dai, S. Zhou and B. Zhang, *Small*, 2022, **18**, e2104550.

35 X. Chen, Q. Li, J. Li, J. Chen and H. Jia, *Appl. Catal., B*, 2020, **270**, 118915.

36 Q. Li, Y. Gao, M. Zhang, H. Gao, J. Chen and H. Jia, *Appl. Catal., B*, 2022, **303**, 120905.

37 K. Bu, S. Kuboon, J. Deng, H. Li, T. Yan, G. Chen, L. Shi and D. Zhang, *Appl. Catal., B*, 2019, **252**, 86–97.

38 H. Song, X. Meng, T. D. Dao, W. Zhou, H. Liu, L. Shi, H. Zhang, T. Nagao, T. Kako and J. Ye, *ACS Appl. Mater. Interfaces*, 2018, **10**, 408–416.

39 Y.-G. Liu, G. Liu, P. Tan, C. Gu, J.-J. Li, X.-Q. Liu and L.-B. Sun, *Chem. Eng. J.*, 2021, **420**, 130490.

40 J. K. Wu, P. Tan, J. Lu, Y. Jiang, X. Q. Liu and L. B. Sun, *ACS Appl. Mater. Interfaces*, 2019, **11**, 29298–29304.

41 O. Dulub, M. Batzill, S. Solovev, E. Loginova, A. Alchagirov, T. E. Madey and U. Diebold, *Science*, 2007, **317**, 1052–1056.

42 D. Wang, H. Shen, L. Guo, C. Wang, F. Fu and Y. Liang, *Appl. Surf. Sci.*, 2018, **436**, 536–547.

43 V. A. Spata and E. A. Carter, *ACS Nano*, 2018, **12**, 3512–3522.

44 Z. Rao, Y. Cao, Z. Huang, Z. Yin, W. Wan, M. Ma, Y. Wu, J. Wang, G. Yang, Y. Cui, Z. Gong and Y. Zhou, *ACS Catal.*, 2021, **11**, 4730–4738.

This journal is © The Royal Society of Chemistry 2022

J. Mater. Chem. A, 2022, **10**, 16016–16028 | **16027**

45 J. Munera, S. Irusta, L. Cornaglia, E. Lombardo, D. Vargascesar and M. Schmal, *J. Catal.*, 2007, **245**, 25–34.

46 Y.-H. Hou, W.-C. Han, W.-S. Xia and H.-L. Wan, *ACS Catal.*, 2015, **5**, 1663–1674.

47 Y. Yang, Y. K. Li, Y. X. Zhao, G. P. Wei, Y. Ren, K. R. Asmis and S. G. He, *Angew. Chem., Int. Ed. Engl.*, 2021, **60**, 13788–13792.

48 P. G. Lustemberg, P. J. Ramírez, Z. Liu, R. A. Gutiérrez, D. G. Grinter, J. Carrasco, S. D. Senanayake, J. A. Rodriguez and M. V. Ganduglia-Pirovano, *ACS Catal.*, 2016, **6**, 8184–8191.

49 X. Jia, X. Zhang, N. Rui, X. Hu and C.-j. Liu, *Appl. Catal., B*, 2018, **244**, 159–169.